J. Fluid Mech. (2022), *vol*. 942, A39, doi:10.1017/jfm.2022.399

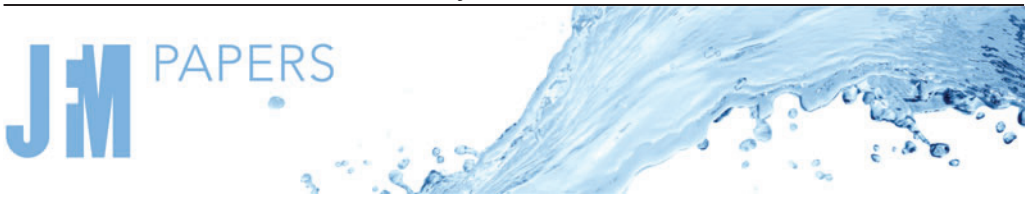

Particle radial velocity and concentration kernels estimation in isotropic grid turbulence experiments of inertialess particles at small separation distances

Si Chen[1], **Pierre-Yves Passaggia**[1,2,3,†] **and Brian L. White**[1,†]

[1]Earth, Marine, and Environmental Sciences Department, University of North Carolina at Chapel Hill, Chapel Hill, NC 27599, USA

[2]University of Orléans, INSA-CVL, PRISME, EA 4229, 45072 Orléans, France

[3]Carolina Center for Interdisciplinary Applied Mathematics, Department of Mathematics, University of North Carolina at Chapel Hill, Chapel Hill, NC 27599, USA

(Received 22 March 2021; revised 23 April 2022; accepted 25 April 2022)

We report experimental measurements of kinematic and dynamic particle concentration kernels conditioned by the separation distances of solid inertialess particles in isotropic turbulence by three-dimensional particle tracking velocimetry with particle diameters smaller than the Kolmogorov length scale. Particle radial relative velocity statistics are measured from the dissipation to the integral length-scale range. The radial scaling of particle and fluid relative velocity variance $\langle w_r(r)^2\rangle \sim r^{2/3}$ in the inertial subrange, consistent with Kolmogorov's theory, is reported, while a new scaling is found for small distances due to finite-size effects between particles. The measured concentration kernels at small separation distances therefore deviate from those in the theory of Saffman & Turner (*J. Fluid Mech.*, vol. 1, 1956, pp. 16–30) at small inter-particle distances due to hydrodynamic interactions. A real kernel taking into account the history of the particle tracks and excluding multiple events is also calculated, while the normalised particle concentration kernels are found to be essentially insensitive to the flow Reynolds number.

Key words: particle/fluid flows, isotropic turbulence

1. Introduction

Particles suspended in a fluid play an important role in several natural and industrial processes. In the atmosphere, collisions of microscopic water droplets in clouds are a necessary step in the production of macroscopic raindrops (Grabowski & Wang 2013),

† Email addresses for correspondence: pierre-yves.passaggia@univ-orleans.fr, bwhite@unc.edu

while collisions of dust grains in turbulent protoplanetary disks are essential in planetesimal formation (Pan & Padoan 2014). Inhomogeneous concentrations of particles in a sandstorm can also dramatically increase the strength of the storm (Carneiro *et al.* 2013). In the ocean, collision and coagulation between suspended phytoplankton cells play an important role in marine aggregate formation (Kiørboe, Andersen & Dam 1990). In industry, examples include solid–liquid separation in wastewater treatment, design of fine spray combustion nozzles, control of industrial emissions (pollutant transport) and titanium dioxide production (Flagan & Seinfeld 1988; Xiong & Pratsinis 1991; Wang, Wexler & Zhou 1998).

Processes associated with inhomogeneous concentrations often involve two distinct physical problems (Sundaram & Collins 1996): the microphysical problem involving particle collisions, which is dependent on the particle/fluid flow conditions; and the macrophysical problem, which involves particle coagulation, preferential concentration and the evolution of particle size and population (Delichatsios & Probstein 1975; Kiørboe *et al.* 1990; Brunk, Koch & Lion 1998*a*,*b*). In this study, we will focus on the microphysical problem of particle conditional concentration rate in turbulent flows based on the separation distance between particles.

Over the past century, particle conditional concentration models for a range of particle inertia and flow conditions have been developed (Meyer & Deglon 2011). Saffman & Turner (1956) in their pioneering work presented a formulation of the geometric conditional concentration kernel for point-like zero-inertia particles in turbulence. In the limiting case where particles have very large inertia, Abrahamson (1975) obtained a simple collision model by arguing that the assumption of independent particle velocities as in gas kinetic theory is appropriate for high-intensity turbulence. The conditional concentration of particles with finite inertia in turbulence is more complicated than the zero-inertia case due to two distinct effects: particle preferential concentration and particle relative velocity (Maxey 1987; Squires & Eaton 1991; Zaichik & Alipchenkov 2009; Pan & Padoan 2010; Gustavsson & Mehlig 2011; Bragg & Collins 2014*a*,*b*; Hammond & Meng 2021).

To date, though, collision kernels for finite-size inertialess particles have not been measured in an experiment, and only the direct numerical simulations (DNS) from Wang *et al.* (1998) and Ten Cate *et al.* (2004) have shown that hydrodynamic interactions can lead to important effects. In particular, the lubrication forces are known to be the dominant repulsion force for this particular regime, which prevents particles from approaching one another when near contact (Ababaei *et al.* 2021). To the best of our knowledge, inertialess particles with a finite size (but smaller than the Kolmogorov length scale) is a regime where experiments have not been yet performed. In this paper, we measure conditional concentration and relative velocity kernels but we are not able to perform measurements for relative distances between particles smaller than one diameter. Therefore, we cannot directly conclude on the collision kernel but provide important information on the concentration of particle pairs conditioned on their separation distance.

Conditional concentration kernels can be described as the average volume of fluid or solid entering a sphere per unit time (Saffman & Turner 1956), and the radius of this sphere sets the separation distance between two particles. Note that when the separation distance is equal to the diameter of the particles, the latter are in contact and the concentration kernel reduces to the collision kernel.

However, in order to draw a link between conditional concentration and collision, it is important also to take into account the time history of particle pairs in order to differentiate the first event when the inter-particle distance falls below a certain threshold (often

denoted as 'geometric') from multiple events (often denoted as 'ghost', resulting from particle–particle interactions). In other words:

(i) For ghost conditional concentration, two particles are considered when their radial distance is lower than a given threshold, but this method does not take into account the time history between two particles where multiple collisions can occur.
(ii) Geometric conditional concentration reintroduces the temporal history between two particles and only considers the first instance as valid.

However, the only way to isolate geometric from ghost conditional concentration is to consider long-enough particle tracks in order to analyse the temporal history of particle pairs. This is one of the novel aspects in the present study compared to the recent experimental work of Hammond & Meng (2021).

Different kernels have been introduced in the present study:

(i) The kinematic kernel (Γ^K) provides a unique perspective to describe the relationship between the particle conditional concentration rate and two statistical properties of the particle phase: the radial distribution function (RDF) and the particle relative velocity (RV). This estimate of the conditional concentration rate in turbulence does not exclude ghost events.
(ii) The dynamic kernel (Γ^d_{gh}) can be defined as the ratio of particle pairs below a certain threshold to particle pair concentration (Rosa *et al.* 2013). It can be obtained by measuring instantaneous particle distances for a given volume and time, and does not exclude multiple events.
(iii) The geometric collision kernel (Γ^d_{re}) is based on the history of particle tracks, which therefore allows for filtering out multiple events.

Note that the kinematic conditional concentration kernel can also be computed such that only the first (initial) event is retained, which should provide similar results to those for the geometric concentration kernel.

Experimental measurements of particle collision is challenging. Most of the relevant literature focuses on the kinematic properties of particles in order to predict conditional concentration kernels. For example, the review by Monchaux, Bourgoin & Cartellier (2012) compares various indicators and methods developed to analyse preferential concentrations of inertial particles in turbulence, including the clustering index, the box counting method, the correlation dimension, the RDF and Voronoï diagrams, to name only a few (Monchaux, Bourgoin & Cartellier 2010, and references therein). Amongst these methods, the RDF is the indicator directly related to the particle conditional concentration kernel (Sundaram & Collins 1996; Wang, Wexler & Zhou 2000). Both three-dimensional (3-D) volumetric techniques such as holographic particle image velocimetry (HPIV) (Meng *et al.* 2004; Cao *et al.* 2008) and lower-dimensional projections such as two-dimensional (2-D) imaging (Peterson, Baker & Coletti 2019) have been applied to the measurement of RDF. However, Holtzer & Collins (2002) demonstrated that the lower-dimensional RDF showed a fundamentally different distribution function than its 3-D counterpart, especially for small particle separation distances. Computing 3-D RDF based on dimensional reduction is not well posed unless a functional form for the 3-D RDF is assumed.

When it comes to particle relative velocity measurement, techniques include HPIV (de Jong *et al.* 2010), 3-D particle tracking velocimetry (3-D PTV) (Bewley, Saw & Bodenschatz 2013; Saw *et al.* 2014) and planar four-frame PTV (Dou *et al.* 2018*a*,*b*).

The first two methods provide 3-D measurement of particle relative velocity; the HPIV method shows significant discrepancies in the tails of the probability density function (p.d.f.) of particle relative velocities compared with DNS, which is attributed to increased ambiguities in the particle matching for larger relative velocities (de Jong *et al.* 2010). The 3-D PTV and four-frame PTV techniques provide comparable accuracy of particle relative velocity measurement; the four-frame PTV is a 2-D technique whose out-of-plane component of particle velocity is lost when projected onto an imaging plane (Dou *et al.* 2018*b*). This problem was very recently addressed by Hammond & Meng (2021) who performed four-pulse particle image velocimetry (PIV) and measured simultaneously the RDF and the RV in a homogeneous and isotropic flow for inertial particles for separation distances of the order of the particle size. In this paper, we explore similar properties for inertialess particles and report the effect of the turbulent Reynolds number and finite particle size.

In this study, we use 3-D PTV and OpenPTV (http://www.openptv.net) software (Maas, Gruen & Papantoniou 1993) to measure both kinematic and dynamic concentration kernels of near-zero-inertia solid particles in isotropic turbulence for separation distances that are small but larger than the sphere's diameter. We compare the measured concentration kernels with the Saffman & Turner (1956) prediction, which does not take into account hydrodynamic interactions induced, for instance, by the motion of the fluid around the particle, which is known to alter particle–particle interactions (Ababaei *et al.* 2021). The aim is to obtain a dynamic kernel and thereby estimate real particle conditional concentration potentially leading to collisions in turbulence. Moreover, based on the method used in the present study, we are able to isolate geometric particle conditional concentration from their ghost counterparts. The paper is organised as follows. The experimental apparatus of PIV and 3-D PTV and the characteristics of the turbulent flows are presented in § 2. The methods of dynamic and kinematic kernel measurements are also described in § 2. Results and discussions are given in § 3 and conclusions are drawn in § 4.

2. Methods

2.1. *Experimental set-up*

The experimental study consists of two complementary techniques using the same flow apparatus. The characteristics of turbulent flow were first quantified by double-frame/single-exposure two-dimensional two-velocity-components (2-D 2-C) PIV. Separate experiments use 3-D PTV to obtain particle trajectories in order to estimate conditional concentration kernels for separation distances greater than or equal to the particle's diameter. The experimental apparatus shown in figure 1(*a*) includes a rectangular tank of 18 cm $\times$ 18 cm $\times$ 22 cm height (inner dimensions) and a horizontally oriented grid attached to a linear motor. Both the tank and the grid are made of clear acrylic sheet of 6.4 mm thickness. The porosity of the grid is 36 %, where the mesh size is $M = 36$ mm and the bar size is $b = 7.2$ mm. The distance of the bars' end from the wall is 0.5 mm, and the set-up is symmetric in both the x and y directions, as shown in figure 1(*a*) (see Chen (2020) for further details). A coordinate system was defined with the origin at the geometric centre of the tank (top view) and 60 mm away from the bottom of the tank; X and Y represent horizontal and vertical directions, respectively. It was defined such that the PIV coordinate system coincides with that of the PTV.

In the PIV system, the light source is a Nano L 135-15 pulsed Nd:YAG laser from Litron Lasers, outputting a light beam at 532 nm, and generating a vertical laser

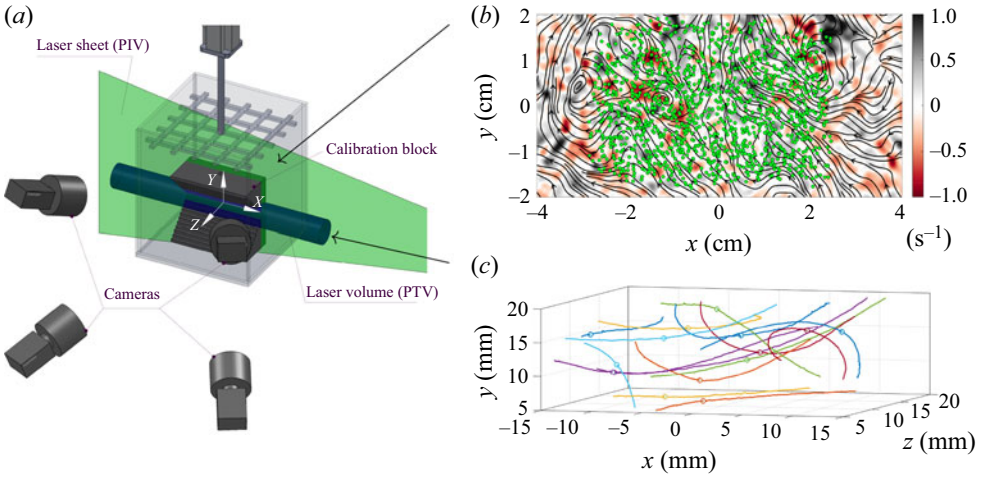

Figure 1. (*a*) The 3-D PTV set-up. (*b*) PTV particles (green) superimposed onto an instantaneous snapshot of vorticity ω_z (red/black) and local streamlines (continuous lines). Note that PIV and PTV were performed in separate experiments and that the present picture illustrates the density of particles with respect to the scales of flow features. In addition, particles are accumulated in the z direction, which gives an impression of high density. However, experiments are performed in the dilute regime and the solid fraction is of the order of 10^{-5}. In the present study, PIV is used to compute flow quantities such as isotropy and dissipation while PTV is used to compute particle relative velocity variance, radial distribution functions and conditional concentration kernels. In panel (*b*), particles were made larger than their real counterpart to appear visible and highlight the volume of measurement of the PTV. (*c*) The 3-D trajectory samples in the volume shown in (*a*) with particle tracks longer than 250 frames. Measurements in both panels (*b*) and (*c*) were performed for the flow condition III (see table 1).

sheet through the centre of the tank. LaVision Glass Hollow Spheres 110P8 (density 1.10 ± 0.05 g cm^{-3}, and mean size 9–13 μm) were used as seeding particles. The instantaneous PIV images were captured by an IMPERX B3320-8MP charge-coupled device (CCD) camera (3312 pixel × 2488 pixel) equipped with a Nikon Nikkor-O Auto 35 mm $f/2$ lens. The camera was synchronised with the laser at a frame rate of 1 Hz with a delay of 0.25 ms between two successive frames. Synchronisation with the laser was performed using a DG535 pulse generator. The software Stream Pix 7 was used for data stream acquisition. The image pairs were processed with DPIVSoft-2010 (Meunier & Leweke 2003; Passaggia, Leweke & Ehrenstein 2012; Passaggia *et al.* 2020) by means of interrogation windows with dimensions 64 pixel × 64pixel for the first pass and 32 pixel × 32 pixel for the second pass with 50 % overlap. The spatial resolution is approximately 43.4 μm pixel^{-1}. The dimensions of the field of view are 14.4 cm × 10.8 cm. Three different turbulent intensities were generated by varying the frequency (f) of the imposed oscillations (1 Hz, 1.5 Hz and 2.5 Hz) with a fixed oscillating stroke of 4 cm, while statistics were obtained by averaging over 750 realisations. The isotropy ratio $u_{1,rms}/u_{2,rms}$ measured using PIV provided values between 0.8 and 1.3, indicating a good degree of isotropy for the three flow conditions. The normalised root-mean-square (r.m.s.) velocities (Hwang & Eaton 2004) are $u_{1,rms}/\overline{u_{1,rms}} \approx 0.9$–$1.2$ and $u_{2,rms}/\overline{u_{2,rms}} \approx 0.8$–$1.3$. Although the velocity field in the vertical direction is slowly decaying, it still can be seen as nearly homogeneous in the region of interest. The turbulent kinetic energy dissipation rate (ϵ) was estimated by means of a time-averaged turbulent

Parameters	Units	Condition I	Condition II	Condition III
Oscillating frequency, f	Hz	1.0	1.5	2.5
Maximum grid velocity	mm s^{-1}	160	240	400
Integral length scale, $\mathcal{L}_{11}$	mm	104	110	120
Taylor microscale, λ	mm	11.8	10.8	9.1
Kolmogorov length scale, η	mm	0.54	0.45	0.32
Kolmogorov time scale, τ_η	s	0.30	0.20	0.10
Turbulent energy dissipation rate, ϵ	m^2 s^{-3}	1.1×10^{-5}	2.49×10^{-5}	9.15×10^{-5}
Turbulent kinetic energy, k	m^2 s^{-2}	1.54×10^{-4}	2.9×10^{-4}	7.51×10^{-4}
R.m.s. turb. vel. fluctuation, $u' = \sqrt{2k/3}$	mm s^{-1}	10.1	13.9	22.3
Kolmogorov velocity scale, u_η	mm s^{-1}	1.0	2.2	3.1
Particles' mean terminal velocity, u_0	mm s^{-1}	0.05	0.05	0.05
Taylor microscale Reynolds number, Re_λ	—	120	150	202
Dissipation scaling, $C_\epsilon = \epsilon\mathcal{L}_{11}/u'^3$	—	1.09	1.01	0.98

Table 1. Driving parameters and turbulent flow characteristics.

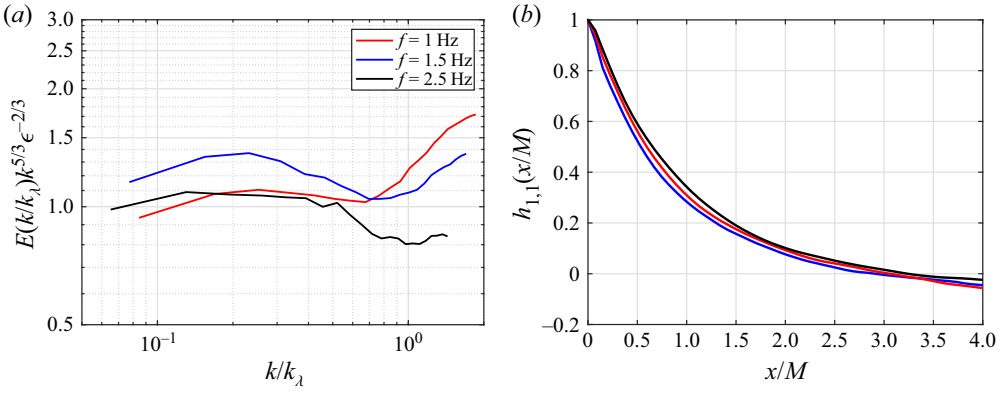

Figure 2. (a) Normalised horizontal velocity spectra from PIV measurements, where $k_\lambda = 2\pi/\lambda$ is the Taylor microscale wavenumber. (b) Autocorrelation function $h_{1,1}(x/M)$ for the three different flow cases.

kinetic energy budget from the PIV data, detailed in Appendix A (see table 1 for the computed values).

The turbulent spectrum was then computed from the PIV data, and the compensated horizontal energy spectrum $E_{11}k^{5/3}\epsilon^{-2/3}$ is shown in figure 2(a) for the three flow conditions. The compensated spectra are essentially flat, confirming the existence of an inertial range for all flow conditions. The horizontal axis is normalised with the Taylor microscale (λ) computed as $\lambda = \sqrt{10\nu k/\epsilon}$, where k is the mean turbulent kinetic energy estimated as $k = 3(u'^2_{rms} + v'^2_{rms})/4$ and ν is the kinematic viscosity of water. The turbulence Reynolds number is $Re_\lambda = u'(\lambda/\nu)$, where $u' = \sqrt{2k/3}$ is the r.m.s. of the velocity fluctuations and provides values $Re_\lambda = [120, 150, 202]$ for the three oscillating frequencies. Note that the lowest value of Re_λ is relatively close to that from the DNS of Ten Cate *et al.* (2004) with similar particles.

In addition, the horizontal autocorrelation function of velocity fluctuations $h_{1,1}(x/M)$ was calculated in order to estimate the horizontal integral length scale $\mathcal{L}_{11}$ and is reported in figure 2(b). This $\mathcal{L}_{11}$ was calculated from the zero crossing of $h_{1,1}(x/M)$ and

slowly increases with the oscillating frequency as reported in table 1. The Kolmogorov equilibrium number $C_\epsilon = \epsilon \mathcal{L}_{11}/u'^3 \approx 1$ was found to be nearly constant and close to the mean value observed in the compensated spectra reported in figure 2(*a*). Note that, in our experiments, $C_\epsilon \approx 1$ is close to the canonical value of 0.9 (Vassilicos 2015). For the lower value of Re_λ, a residual large-scale circulation exists but its amplitude with respect to turbulence kinetic energy decreases with increasing stroke frequency f. This mean flow is composed of large-scale circulation regions whose amplitude is stronger in the bottom and decreases closer towards the grid. In the region where PTV measurements are performed, the mean velocity $\sqrt{K}$ (where K is the mean flow kinetic energy) is roughly half the r.m.s. of the turbulent kinetic energy in this region. The resulting ratio between the mean-field kinetic energy and the turbulent kinetic energy is 0.27 for the worst-case scenario when $f = 1$ Hz and decreases to 0.19 for $f = 2.5$ Hz.

A schematic of the 3-D PTV and planar two-component PIV set-up is shown in figure 1(*a*). The 3-D PTV imaging system consists of four synchronised Grasshopper3 3.2 MP cameras. A continuous-wave argon ion laser was used to generate a cylindrical laser volume of 4 cm diameter through the tank. During PTV experiments, the tank was first filled with pre-filtered saline solution. The calibration process was then conducted to determine the interior and exterior parameters of the cameras, the lens distortions and electronic effects (Maas *et al.* 1993). To quantify uncertainty in the calibration process, the real positions of points on the calibration block were compared with the positions measured from PTV (Akutina 2016), and the r.m.s. of the errors obtained were $\text{r.m.s.}_x = 0.0203$ mm, $\text{r.m.s.}_y = 0.0244$mm and $\text{r.m.s.}_z = 0.0240$ mm. Quasi-monodisperse polyethylene microspheres (Cospheric LLC) with density $\rho_p = 1.084$ g cm^{-3} (the same as the density of saline solution ρ_f) and diameter range $D =$ 106–125 μm were used for PTV and, for each flow condition, 0.15 mg of particles were used consisting in a dilute volume fraction $O(10^{-5})$. The particle Stokes number, $St \equiv \tau_p/\tau_\eta$, the ratio of the particle response time $\tau_p = \rho_p D^2/18\mu_f$ (where μ_f is the fluid dynamic viscosity) to the turbulent Kolmogorov time scale $\tau_\eta = \sqrt{\nu/\epsilon}$, ranges from $St = 0.0028$ to $St = 0.0080$ in the three flow conditions. The particles were allowed to mix for one minute after being dispersed, before data acquisition began. A series of 72 000 images (10 min at 120 frames s^{-1}) per camera were then captured. On average, the number of voxels moved per frame with an acquisition rate at 120 Hz is of the order unity for flow condition I, two voxels for flow condition II, and three voxels for flow condition III, which is the size of an individual particle for the latter (see table 1).

The 3-D PTV data processing performed in OpenPTV can be divided into two major parts: determination of particle positions in spatial coordinates and tracking of individual particles through consecutive images. The approach of Willneff (2003) is used in the present study and combines the two steps together with a spatio-temporal matching method which improves tracking efficiency of particles by 10–30 % (Lüthi, Tsinober & Kinzelbach 2005). Willneff's method predicts particle motion based on particle tracking in image and object space to resolve ambiguous particle image positions and correspondences. In other words, 'temporal' information at time t is used to resolve 'spatial' uncertainties regarding the existence and positions of particles in the next time step $t + \Delta t$. The seemingly modest improvement of 10–30 % in tracking efficiency is very significant in the context of further processing and analysis. Particle trajectories that are longer than the relevant Kolmogorov scales, η and τ_η, are the key prerequisite for a Lagrangian flow analysis, and they also significantly enhance the accuracy of the applied processing to obtain velocity derivatives (Lüthi *et al.* 2005). To track particles, i.e. to find corresponding particles in image and

object space of consecutive time steps, three criteria are used for effective assignment. First, a 3-D search volume is defined by minimum and maximum velocities in all three coordinate directions. Second, the Lagrangian acceleration of a particle is limited, defining a conic search area. Third, in the case of ambiguities, the particle leading to the smallest Lagrangian acceleration is chosen. Similarities in brightness, width, height and sum of grey values of the pixel of a particle image in two consecutive time steps proved to be not as valuable as expected. From the 565 detected particles per frame for which a position in space can be determined, typically 470 particles can be followed long enough, which is equivalent to a tracking efficiency of $\sim$80 % and a seeding density for linked particles of $\sim$26 particles cm^{-3}.

An instantaneous vorticity ω_z and some 3-D trajectory samples at $f = 2.5$ Hz (i.e. flow condition III) are shown in figures 1(*b*) and 1(*c*), respectively. Figure 1(*b*) illustrates the particle density accumulated in the out-of-plane direction as well as the size of the relevant scales in the experiment. Note that both results were acquired in separate experiments.

2.2. *Conditional concentration kernel models*

The collision rate between particles in a monodisperse system can be described as (Wang *et al.* 1998)

$$\mathcal{N}_c = \Gamma^d \frac{\bar{n}^2}{2}, \tag{2.1}$$

where $\mathcal{N}_c$ is the collision rate per unit volume and $\bar{n}$ is the particle number concentration, defined as N_p/Ω, where N_p is the number of particles and Ω is the observation volume. The dynamic kernel Γ^d, namely the ratio of concentration rate conditioned based on the distance d to particle pair concentration (Rosa *et al.* 2013), can be obtained by directly measuring N_p, Ω and the number of events when particles are separated by a certain distance d over time. The conditional concentration is obtained by counting the number of particles located at a distance smaller than or equal to a given inter-particle distance $d > D$, which is then averaged in time. In what follows, we report conditional concentrations down to $d/D = 2$. The associated error level is dependent only on the number of events measured during the experiment and is below 5 % for all cases considered in the present study.

In the pioneering work of Saffman & Turner (1956), the conditional concentration kernel was described as the average volume of fluid entering a sphere per unit time. Saffman & Turner showed that this kernel for zero-inertia particles can be written as

$$\Gamma(d) = 2\pi d^2 \langle |w_r(d)| \rangle, \tag{2.2}$$

where $d \geqslant D$ is the distance between two particles. The particle pair radial relative velocity $w_r(d)$ at a separation distance d is defined as $w_r(d) = (\boldsymbol{v}_2 - \boldsymbol{v}_1) \cdot \boldsymbol{d}/|\boldsymbol{d}|$ (Dou *et al.* 2018*b*). The subscript r means 'radial' and, since the velocity component perpendicular to the separation vector is not relevant to the particle conditional concentration nor collision, we will refer to radial relative velocity as 'relative velocity' from here on. Here $\boldsymbol{v}_2$ and $\boldsymbol{v}_1$ are the velocities of particles 1 and 2, $\boldsymbol{d}/|\boldsymbol{d}|$ denotes the unit vector in the direction parallel to the separation vector, and $\langle \cdot \rangle$ denotes the ensemble average. Further assuming that $d \ll \eta$, uniform particle concentrations in space and probability distributions of the velocity gradient being Gaussian, Saffman & Turner (1956) proposed the following expression for

the conditional concentration kernel in turbulent flows:

$$\Gamma^{ST}(d) = 1.294 d^3 \left(\frac{\epsilon}{\nu}\right)^{1/2}. \tag{2.3}$$

Note that this concentration kernel reduces to the collision kernel when $d = D$, that is, when the separation distance is equal to one diameter.

The theoretical description of $\Gamma(d)$, (2.2), was then further developed by Sundaram & Collins (1997) to take into account non-uniform particle spatial distribution:

$$\Gamma^{K}(d) = 4\pi d^2 g(d) \langle w_r(d)^- \rangle, \tag{2.4}$$

where $g(d)$ is the RDF, which serves as a correction to the particle number concentration due to non-uniform particle distribution. Here, $\langle w_r(d)^- \rangle$ represents the inward particle radial relative velocity, which relates to particle pairs moving towards one another. The inward radial relative velocity can be further expressed as (Sundaram & Collins 1996)

$$\langle w_r(d)^- \rangle = \int_{-\infty}^{0} -w_r P(w_r \mid d)\, \mathrm{d}w_r, \tag{2.5}$$

where $P(w_r \mid d)$ is the p.d.f. of w_r conditioned on the inter-particle distance d. The kinematic conditional concentration kernel Γ^K, (2.4), thus combines the effects of the particles' relative motion and particles' preferential concentration.

2.3. *Conditional concentration kernel measurements*

In order to determine dynamic conditional concentration kernels for small separation distances, the present study considers the method introduced in Balachandar (1988) and Wang *et al.* (1998) to detect inter-particle distances. The analysis mainly focuses on geometric particle overlap for a given separation distance.

Inter-particle distance corresponding to collisions (i.e. when $d = D$) is particularly challenging in laboratory experiments. The time scale associated with physical collisions of real particles (i.e. $D \approx 0.116$ mm in the present study) is much smaller than the temporal resolution of the experimental set-up (Yang & Hunt 2006; Monchaux *et al.* 2010; Marshall 2011; Ababaei *et al.* 2021). Instead, we consider analogous particles (Hill, Nowell & Jumars 1992), which are fluid volumes centred on real particles with effective diameters larger than D. The conditional concentration detection was thus based on the effective particle diameters d (which are adjustable) to obtain a relationship between conditional concentration kernels and thereby analogous collision kernels versus effective particle diameter. A schematic of effective diameters is shown in figure 3(*a*). Care should be taken to ensure that the effective diameters are small enough that the analogous particles can still be seen as inertialess and follow the fluid (and their host particles') motion faithfully. The conditional concentration kernel derived using the 'ghost events' approximation will be denoted as Γ^d_{gh}. This method counts all possible inter-particle distances below a given threshold but does not take into account the nature of the particles' relative motion. A more realistic scheme is also considered: in the case of a particle pair candidate, if there are multiple points along the trajectories when two particles approach one another with distances smaller than their effective diameter (i.e. a multiple conditional concentration event), only the first instance meeting the threshold is considered. This conditional concentration kernel is denoted as Γ^d_{re}.

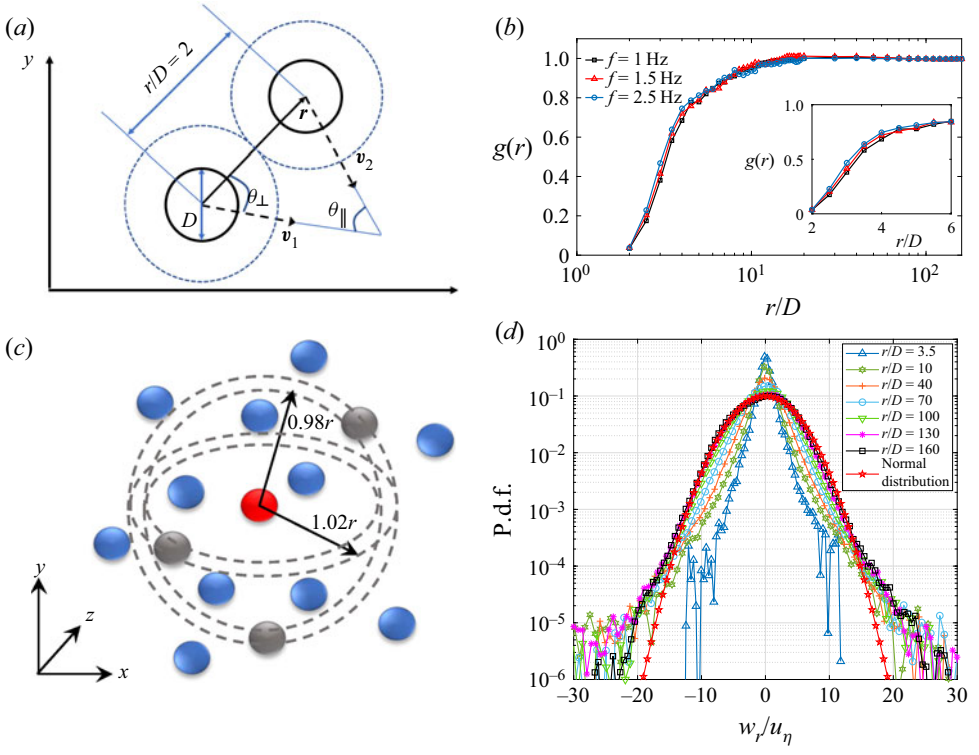

Figure 3. (*a*) Sketch of the particle coordinate system, distances and angles used in the analysis. Analogous particle conditional concentration events are shown with dashed lines. (*b*) Time-averaged RDF measured under three flow conditions. The distance is normalised by the particle diameter. (*c*) Sketch of the measurement method of the radial distribution function. Particles in grey are in the range $d = [0.98r, 1.02r]$ from the red particle, while the blue particles are out of that range. (*d*) P.d.f.s of particle pair radial relative velocity conditioned on different separation distances at 2.5 Hz. The particle relative velocities are normalised by the Kolmogorov velocity scale u_η. The p.d.f. of the standard normal distribution is also given for comparison.

For the kinematic conditional concentration kernel, the RDF is calculated by the following expression (McQuarrie 1976; de Jong *et al.* 2010):

$$g(r_i) = \frac{N_i/\Delta V_i}{N/V}. \tag{2.6}$$

At each time step of the experiment, an arbitrary particle's location is taken to be at the origin O. In the above, N_i is the number of particles that lie within a range of $[0.98r_i, 1.02r_i]$ relative to this origin (a spherical shell), r_i is the average radius of the spherical shell, ΔV_i is the volume of the spherical shell, i is the discrete index, and N/V is the average particle number concentration. The RDF $g(r_i)$ is averaged over all the cases in which each particle takes a turn to serve as the origin and then averaged again over time. A sketch of the way the RDF is calculated is shown in figure 3(*c*). Periodic boundary conditions are used to cope with the reduction of the number of particles at larger particle separation distances (de Jong *et al.* 2010).

Figure 3(*b*) shows the time-averaged RDF measured for the three flow conditions with separations from less than the Kolmogorov length scale to the integral length scale. In the case of inertialess particles in turbulence, there is no preferential concentration and the RDF should equal unity. However, when the particle separation $d/D < 5$, the RDF is

smaller than 0.8 (see figure 3*b*). This result can seem surprising at first, since most studies analysed inertial particles, which tend to collide. For inertialess particles, the picture is somewhat different, since hydrodynamic effects can prevent particles coming near contact and can span large inter-particle distances because of the viscous nature of the flow. The recent DNS of inertial particles in homogeneous turbulence by Ababaei *et al.* (2021) shows that the RDF can drop well below unity when $r/D < 3.5$, $St_k < 0.1$, and when long-range many-body interactions and lubrication forces are taken into account. Thus, it is essential to take $g(r)$ into account when measuring conditional concentration kernels when the separation distance is small, even for inertialess particles. The particle radial relative velocities were collected and binned according to the particle separation distance r with a bin size in the range $[0.98r, 1.02r]$. Ranges $[0.95r, 1.05r]$ and $[0.9r, 1.1r]$ were also tested, but without noticeable differences on the RDF. Then $\langle w_r(d)^- \rangle$ was calculated according to (2.5).

2.4. *Fluid and particle radial relative velocity*

Hereafter, we evaluate the following: (i) the dynamic conditional concentration kernel Γ^d by directly measuring the number of particles for separation distances lower than d, the volume these particles occupy and the number of events; (ii) the kinematic conditional concentration kernel Γ^K through (2.4) by measuring $\langle w_r(d)^- \rangle$ and the RDF at different effective diameters; and (iii) the Saffman & Turner (1956) concentration kernel Γ^{ST} through (2.3) by measuring the turbulent energy dissipation rate ϵ, and we provide a comparison. (iv) We also use the second-order relative velocity structure functions of particles $S^P_{2\parallel} \equiv \langle w_r(r)^2 \rangle$, following the nomenclature in Bragg & Collins (2014*b*) and assuming that particles strictly follow fluid particles.

We use the second-order relative velocity structure functions for the fluid $S^f_{2\parallel}$ as a reference to deduce the scaling laws of particle motions and determine the behaviour of $S^P_{2\parallel}$. According to Kolmogorov theory, the second-order relative velocity structure function is given by

$$S^f_{2\parallel} = \begin{cases} \dfrac{\epsilon}{15\nu} r^2, & \text{for } \eta < r < \lambda, \\ C_2(\epsilon r)^{2/3}, & \text{for } \lambda \ll r \ll \mathcal{L}_{11}, \\ 2(u'^2), & \text{for } r > \mathcal{L}_{11}, \end{cases} \tag{2.7}$$

where C_2 is a constant, u'^2 is the mean turbulent velocity fluctuation squared and $\mathcal{L}_{11}$ is the integral length scale, measured using the autocorrelation method from the PIV and found to be nearly constant among the flow conditions at each location considered. In what follows, we show that, for small distances, finite-size effects can play an important role in determining the p.d.f. of particle relative velocity and their second-order structure function.

3. Results and discussion

In this section we analyse the statistical properties of relative particle motions across multiple scales, from the integral length scale characterising the mean size of the large eddies of turbulence down to below the Kolmogorov scale. We begin with the p.d.f.s of particle pair radial relative velocity conditioned on different separations for flow condition III in figure 3(*d*) and observe a remarkable deviation from the Gaussian distribution, particularly at small separation distances.

At large separation distances, the p.d.f.s of relative velocity are slightly negatively skewed, which is a natural consequence of vortex stretching in turbulence (Tavoularis, Bennett & Corrsin 1978). For smaller separations (figure 3*c*), the p.d.f.s become symmetric, which is in line with the relative velocity p.d.f.s of Saw *et al.* (2014), who did not observe significant skewness in their relative velocity p.d.f.s at $r/\eta \approx 1$ for inertialess particles; the tails of our relative velocity p.d.f.s are somewhat higher but much lower than reported in Hammond & Meng (2021) for inertial particles. The essentially straight tails for $r/D = 3.5$ hint at a decrease of the particles' relative motion, contrary to finite-Stokes-number particles where the tails of the p.d.f.s are wide. This further hints at the importance of particle–particle interactions for scales of the order of the particle size, and we analyse the motion of two finite-size inertialess particles using the structure function method together with asymptotic theory for the lubrication motion of two colliding particles.

3.1. *Radial relative velocity variance and finite-size effects*

The second-order particle relative velocity structure functions (i.e. particle relative velocity variance) $S^P_{2\parallel}$ normalised by the square of Kolmogorov velocity scales u^2_η are shown in figure 4(*a*). A feature of $r^{2/3}$ scaling in the inertial subrange is observed for $r > \lambda$, consistent with Kolmogorov theory in (2.7). The transitions between the viscous and the inertial subranges should scale as r^2 but exhibits a plateau in the range $\eta > r \gtrsim \lambda$ for flow conditions I and II. This is attributed to the effects of low Taylor Reynolds number and a loss of isotropy at these scales (see Kim & Antonia 1993) and the relatively small distance from the oscillating grid. For flow condition III, this region becomes slightly steeper and the plateau progressively disappears. Note that the same behaviour was observed in the particle-resolving DNS of Ten Cate *et al.* (2004) for similar Taylor Reynolds numbers and inertialess particles. As the radial distance approaches the integral length scale, the normalised particle relative velocity approaches a plateau defined by the energy-containing scale $\mathcal{L}_{11}$ given by the velocity structure function (2.7). However, due to the relatively short distance from the grid and the presence of the large-scale circulation, we obtain a prefactor close to 0.9 instead of 2 in this expression for the flow condition I. The prefactor increases to 1.4 for the flow condition III.

For $r < \eta$, the relative velocity should abruptly drop to zero. However, the decay for $S^P_{2\parallel}$ is different from what was anticipated for $S^f_{2\parallel}$ and hints at particle–particle interaction. This can also be observed in figure 10 in Ten Cate *et al.* (2004) when plotted with logarithmic scales, which we report in our study for comparison and analysis (see figure 4*b*). A similar trend was also reported very recently in the DNS of Ababaei *et al.* (2021) at high Taylor Reynolds numbers for inertial particles when long-range many-body interactions and lubrication effects were taken into account. Therefore, we analyse a new weaker scaling (see figure 4*a*) that accounts for the onset of combined effects of lubrication forces and finite-size effects since the motion of the fluid should not influence relative inward velocity for $r < \eta$.

In the low Reynolds-number regime for a spherical particle moving in a fluid, where the particle Reynolds number $Re_p = u_\eta D/\nu \ll 1$, Mongruel *et al.* (2010) proposed a model based on a second-order ordinary differential equation describing the temporal evolution of the particle–particle distance for two particles moving towards one another, assuming that lubrication is the dominant effect.

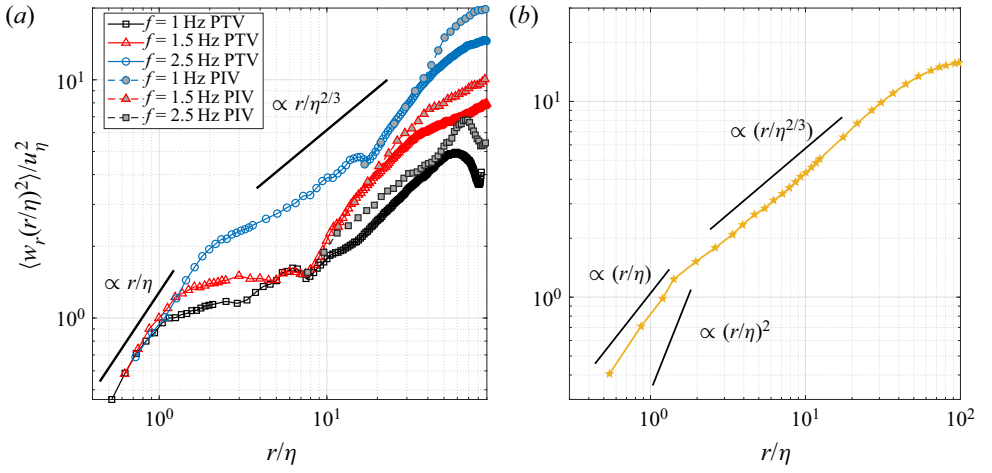

Figure 4. (*a*) Normalised relative velocity variance from measurements for the particles $S^P_{2\parallel}$ (lines with symbols) acquired from PTV and the fluid $S^f_{2\parallel}$ (dashed lines) acquired from PIV in a separate experiment, with $u_\eta = (\nu\epsilon)^{1/4}$ being the Kolmogorov velocity scale. (*b*) Normalised relative velocity variance $S^P_{2\parallel}$ from the DNS of Ten Cate *et al.* (2004) from their figure 10 but plotted in logarithmic scales exhibiting the same scaling laws as the present experimental study.

Starting from the equation of motion for a sphere approaching a fixed wall, or equivalently for two particles approaching head-to-back vertically (Marshall 2011), the equation of motion becomes

$$m_p \frac{\mathrm{d}V_p}{\mathrm{d}t} = -6\pi R\mu V_p(\delta) f_{rr}(\delta, Re_p) + \frac{4}{3}\pi R^3(\rho_p - \rho_f)g, \tag{3.1}$$

where $\delta = (r - D)/D$ is the gap between two particles, V_p is the particle velocity and $f_{rr}(\delta, Re_p)$ is the friction factor given in Cox & Brenner (1967) as

$$f_{rr}(\delta, Re_p) = \frac{1}{\delta} + \frac{1}{5}\left[1 + \frac{Re_p}{4}\right]\ln\left[\frac{1}{\delta}\right] + O(Re_p^2), \tag{3.2}$$

which diverges when $r - D$ becomes asymptotically small or equivalently $\delta \to 0$. In the region very close to the wall, the velocity growth is modelled at first order by a linear growth with the normalised distance δ (in agreement with experiments (Mongruel *et al.* 2010; Marshall 2011)) of the form

$$V_p = \delta V^m_{St}, \tag{3.3}$$

where V^m_{St} is some characteristic velocity. Keeping only the terms on the right-hand side of (3.1) (i.e. neglecting particle inertia), it follows that in this region we take

$$f_{rr}(\delta, Re_p) = \frac{1}{\delta}\frac{V_{St}}{V^m_{St}}, \tag{3.4}$$

where V_{St} is the Stokes velocity which is chosen equal to $u_\eta = (\nu\epsilon)^{1/4}$, the Kolmogorov velocity scale. In the particular case $Re_p \ll 1$, then $f_{rr}(\delta, Re_p) = 1/\delta$ and from the classical lubrication theory and $V_{St} = V^m_{St}$, it appears appropriate to use V^m_{St} as a velocity scale. We then define a dimensionless time $\tau = tV^m_{St}/R$ then $V_p/V^m_{St} = -\mathrm{d}\delta/\mathrm{d}\tau$. We further assume

that the friction factor f_{rr} can be used in the near-contact case ($\delta \ll 1$). Equation (3.1) is then rewritten in dimensionless form as

$$-St_m \frac{\mathrm{d}^2\delta}{\mathrm{d}\tau^2} = \frac{1}{\delta}\frac{\mathrm{d}\delta}{\mathrm{d}\tau} + 1, \tag{3.5}$$

where $St_m = \rho_p (V_{St}^m)^2/(\rho_p - \rho_f)gR$ is a modified Stokes number for the particle.

Izard, Bonometti & Lacaze (2014) then proposed a modified version of (3.5) where the effective roughness height ζ_e for non-smooth spheres is included. In this case, the lubrication force $\boldsymbol{F}_{lub}$ between two finite-size particles (i.e. a particle i and a particle j) of velocity $\boldsymbol{u}_{pi}$ and $\boldsymbol{u}_{pj}$ and radius R_i and R_j, respectively, can be written as (Brenner 1961)

$$\boldsymbol{F}_{lub} = -\frac{6\pi\mu(\boldsymbol{u}_{pi}\cdot\boldsymbol{n} - \boldsymbol{u}_{pj}\cdot\boldsymbol{n})}{r + \zeta_e}\left(\frac{R_i R_j}{R_i + R_j}\right)^2 \boldsymbol{n}, \tag{3.6}$$

where ζ_e accounts for the mean height of surface asperities of real particles. This allows for mimicking real particles and avoiding the divergence of the force in (3.5) when contact occurs (i.e. $r = D$). The present lubrication force becomes active only when the distance between particles r is such as ($0 \leqslant r \leqslant 2D$). This upper bound is in the range of the critical distance for which the velocity of the particle decreases due to the presence of the wall (see Izard *et al.* 2014, and references therein). Using $\boldsymbol{F}_{lub}$ in (3.6) instead of f_{rr} in (3.4), equation (3.5) becomes

$$St_m \frac{\mathrm{d}^2\delta}{\mathrm{d}\tau^2} + \frac{D}{(r - D + \zeta_e)}\frac{\mathrm{d}\delta}{\mathrm{d}\tau} + 1 = 0. \tag{3.7}$$

Note that this equation remains valid for separation distances smaller than $\eta = 1 \approx 3D$ (Izard *et al.* 2014), even for small gap distances $r \gtrsim D$. In the present model, we obtained $St_m = [0.67, 0.98, 1.18]$, $\zeta_e/R = 0.05$ and $R = 5.5 \times 10^{-5}$ m.

Equation (3.7) is integrated numerically and shown in figure 5(*a*) where the boundary conditions $\delta(r/\eta = 1)$ and $\mathrm{d}\delta(r/\eta = 1)/\mathrm{d}\tau$ are set to the values obtained in figure 4(*a*). Figure 5(*a*) shows a similar behaviour to that reported in the experiment where the scaling for $\langle w_r(r)^2\rangle/u_\eta^2$ is less steep than originally predicted by the second-order structure function for distances smaller than the Kolmogorov length scale. In particular, $\langle w_r(r)^2\rangle/u_\eta^2 \sim r/\eta$ for increasing forcing frequency f, which simultaneously corresponds to increasing the finite-size ratio D/η. In other words, the mean inward velocity variance $w_r(r)$ no longer evolves linearly with the radial distance r but seems to follow a power law. From figure 4(*a*,*b*), the particle structure function $S_{2\parallel}^P$ appears to approach a scaling of the form

$$S_{2\parallel}^P \approx r\epsilon/(15\nu), \quad \text{for } D \lesssim \eta \text{ and } r \leqslant \eta, \tag{3.8}$$

and could be due to lubrication effects, whose consequences perhaps persist at those large distances. A similar behaviour was also recently reported in Ababaei *et al.* (2021) where lubrication effects and long-range many-body interactions were found to decrease the RDF and modify the relative velocity scaling for $r/D < 3.5$ at low but finite Stokes numbers.

This scaling is compared to the numerical integration of (3.7) in figure 5(*a*) and provides a good agreement for all flow conditions. The comparison between measurements and the theoretical model for the inward velocity variance suggests that lubrication effects could be the physical mechanisms leading to the scaling $\langle w_r(r)^2\rangle/u_\eta^2 \sim r/\eta$. Next, we analyse the relative particle angles for separation distances $r \lesssim \eta$.

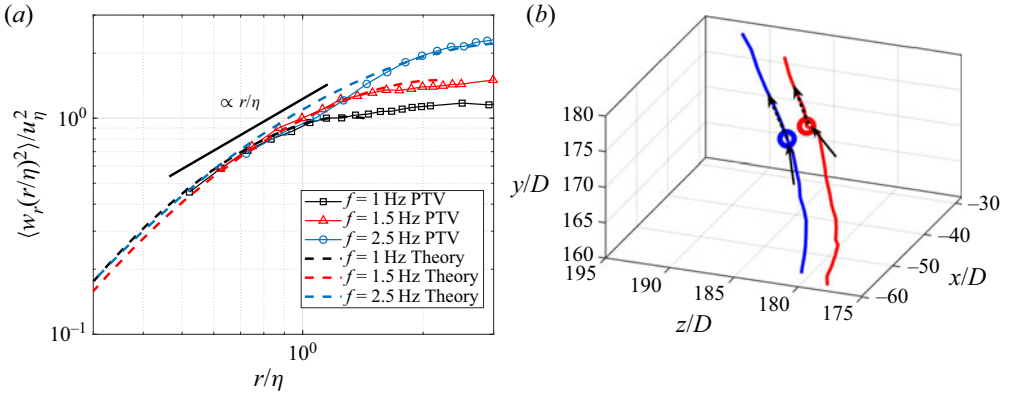

Figure 5. (*a*) Normalised particle relative velocity variance from measurements for $S_{2\parallel}^P$ from the dynamic model (3.7) under three flow conditions. (*b*) Sample trajectories showing two particles near contact measured for $f = 2.5$ Hz and $r/D = 2$.

3.2. *Relative angles at small separation distances*

A characteristic sample of particle tracks is shown in figure 5(*b*) where the separation distance between the two particles is $r/D = 2$ for the flow condition III. It is interesting to see that both tracks follow one another before and after the smallest separation distance. This therefore leads to small relative velocity, in agreement with the interpretation of the p.d.f. shown in figure 3(*d*). The p.d.f. of different angles for small separation distances as a function of both the turbulent Reynolds number and the separation distance r/D are analysed. Here we considered two different angles: the particle tangential velocity angle $\theta_\parallel$ and the particle relative position angle $\theta_\perp$ defined as

$$\cos(\theta_\parallel) = \frac{|\boldsymbol{v}_1 \cdot \boldsymbol{v}_2|}{|\boldsymbol{v}_1||\boldsymbol{v}_2|} \quad \text{and} \quad \cos(\theta_\perp) = \frac{|\boldsymbol{v}_1 \cdot \boldsymbol{r}|}{|\boldsymbol{v}_1||\boldsymbol{r}|}. \tag{3.9a,b}$$

We begin the analysis by representing the particles' tangential velocity angle $\theta_\parallel$ for different flow conditions in figure 6(*a*) and different separation distances r/D in figure 6(*c*), before and after the smallest separation distance. For $r/D = 2.5$, the peak of the p.d.f.s narrows as the forcing frequency is increased and the peak shifts from $\theta_\parallel \approx 22^\circ$ for the flow condition I to a nearly parallel angle $\theta_\parallel \approx 7^\circ$ for the flow condition III. It is interesting to note that, for $r/D = 2.5$, the p.d.f. narrows for every flow condition before and after the smallest separation distance, which shows that hydrodynamic interactions modify the trajectories of the particles. In other words, after the smallest separation distance, the trajectories of the particles tend to align with one another and particles tend to fly along as depicted in figure 5.

The effect of the separation distance is shown in figure 6(*c*) before and after the smallest separation distance, for the flow condition III. While the p.d.f.s are self-similar for $3 \leqslant r/D \leqslant 5$, the smaller separation distance ($r/D = 2.5$) shows that particles tend to further align their trajectory.

The particle relative position angle $\theta_\perp$ is reported for different flow conditions in figure 6(*b*) and different separation distances r/D in figure 6(*d*), similar to figure 6(*a*,*c*). From both plots, it is clear that, near the smallest separation distance, at $r/D = 2.5$, the p.d.f. peaks near $\theta_\perp \approx 85^\circ$ but the distributions flatten as the forcing frequency decreases. The peak also shifts from $\theta_\perp \approx 60^\circ$ for the flow condition I, $\theta_\perp \approx 68^\circ$ for the flow condition II and $\theta_\perp \approx 85^\circ$ for the largest forcing frequency. Similarly, figure 6(*d*) shows

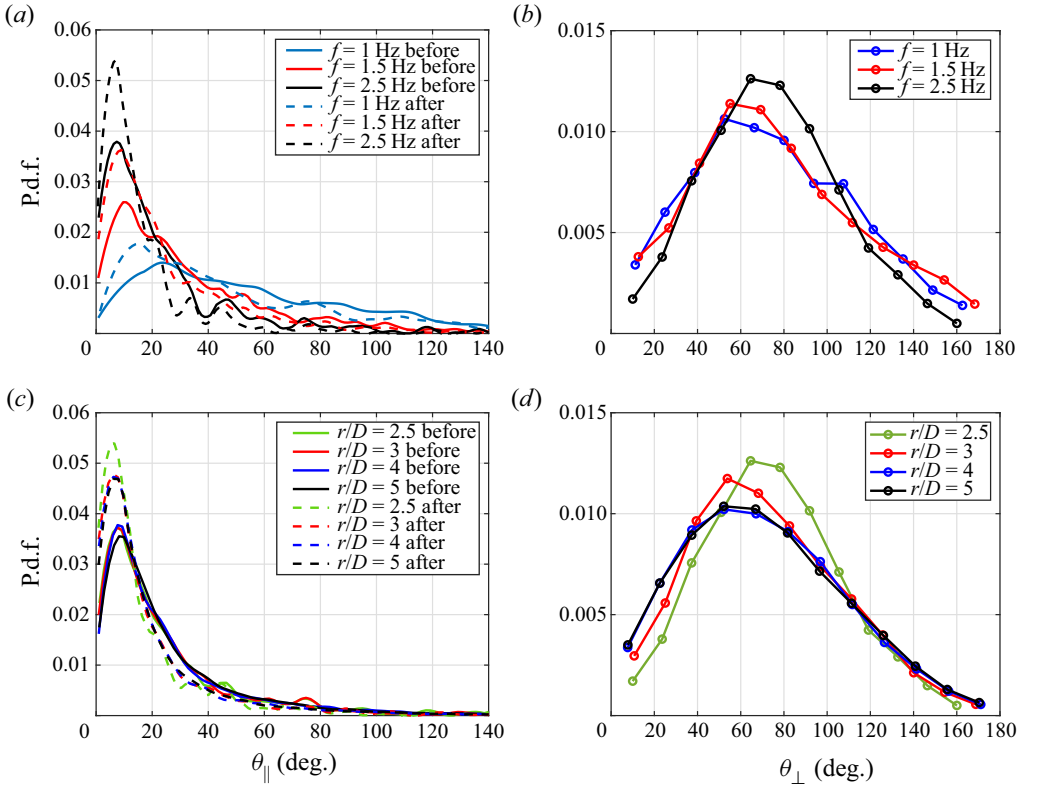

Figure 6. (*a*) P.d.f. of particle tangential velocity angle $\theta_{\parallel}$, measured at $r/D = 2.5$, and (*b*) relative position angle $\theta_{\perp}$ as a function of the grid frequency. (*c*) Same as panel (*a*) but as a function of the separation distance r/D before and after the smaller separation distance. (*d*) Same as panel (*b*) but as a function of r/D measured for $f = 2.5$ Hz.

the effect of the separation distance r/D, where, for $r/D > 3$, the p.d.f.s are essentially self-similar and peak at $\theta_{\perp} \approx 50^{\circ}$. These results are consistent with the DNS results of Wang *et al.* (2006), who analysed relative angles in homogeneous turbulent at low Taylor Reynolds numbers (i.e. up to 55). For $r/D \leqslant 3.5$ the angle tends to increase, which denotes that finite-size effects tend to modify the particle's relative position angle.

The analysis of the tangential velocity and relative position angles seems to confirm that particle pairs tend to follow one another for $2.5 \leqslant r/D \leqslant 5$, with a relative angle in the range 60°–85°. Head-on or head-to-tail scenarios seem unlikely to occur. The fact that p.d.f.s are modified when $r/D \leqslant 3.5$ supports the idea that finite-size effects start to appear for small separation distances and prevent particles from colliding with one another. This is also in line with the fact that the RDF drops below one at small separation distances. Lubrication forces are likely to prevent particles from approaching one another, modifying their relative angle, and decrease the probability to observe particle pairs with small separation distances.

3.3. *Conditional concentration kernels*

Now that the dynamic conditional concentration kernel has been defined and that finite-size effects have been described, we continue with the analysis of the conditional

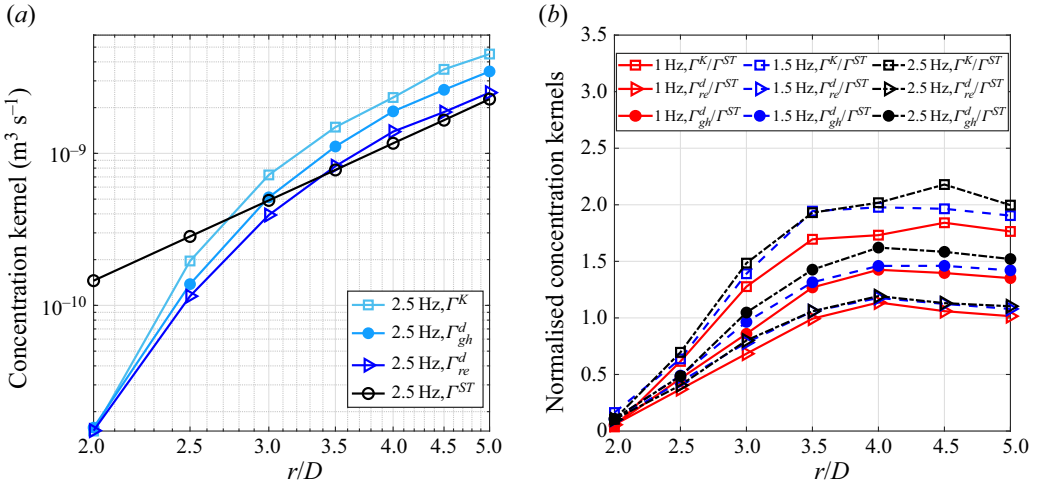

Figure 7. (*a*) Measured conditional concentration kernels Γ^K, Γ^d_{gh}, Γ^d_{re} and Γ^{ST} for flow condition III and (*b*) normalised conditional concentration kernels Γ^K, Γ^d_{gh} and Γ^d_{re} by Γ^{ST} at the three flow conditions.

concentration kernels by comparing direct measurements of the number of events where particles are observed at a given separation distance to the different available theories. In addition, finite-size effects will be found to play a key role in the normalised conditional concentration kernels for small separation distances, as already reported in the DNS of Ababaei *et al.* (2021).

Conditional concentration kernels at small separation distances Γ^K, Γ^d_{gh}, Γ^d_{re} and Γ^{ST} are compared in figure 7(*a*) with the averaged number of particles, observation volumes and particle number concentrations measured and reported in table 2. The observation volumes were measured with a QuickHull algorithm (Barber *et al.* 1996). In figure 7(*a*), only kernels for flow condition III are shown for clarity; Γ^d_{gh}, Γ^d_{re} and Γ^K normalised by Γ^{ST} are shown in figure 7(*b*). We note the following.

(i) The ratio Γ^K/Γ^{ST} decreases monotonically and falls below unity with decreasing separation distance. We attribute this deviation to finite-size effects. As mentioned above, the theory of Saffman & Turner (1956) is based on the assumptions of negligible particle–particle interactions. In the present experiments, the particle separation distance becomes sufficiently small such that particle–particle interactions cannot be ignored. This effect starts to play a role for $r/D \leqslant 3.5$, as shown in figure 7. As the separation decreases and particles approach one another, finite-size effects act against particles' collision, leading to a decrease in Γ^K compared with Γ^{ST}.

As r/D increases, finite-size effects become negligible and the ratio Γ^K/Γ^{ST} becomes nearly constant. Saffman & Turner assumed that the probability distribution of the velocity gradient is Gaussian; however, the p.d.f. of particle pair radial relative velocity, shown in figure 3(*d*), is indeed not Gaussian at small distances. The finite ratio of particle size to Kolmogorov length scale leads to a larger particle relative velocity than that of fluid particles, which contributes to a larger Γ^K.

	Condition I	Condition II	Condition III
Average number of particles, $\overline{N_p}$	608	765	764
Average observation volume, $\overline{\Omega}$ (cm^3)	29.8	29.5	29.3
Average particle number concentrations, $\overline{N_p}/\overline{\Omega}$ (cm^{-3})	20.4	25.9	26.0
Stokes number, $St_k = (\rho_p D^2/18\mu)/\tau_\eta$	0.0028	0.0042	0.0080
Kolmogorov length scale to particle diameter, η/D	4.7	3.9	2.8

Table 2. Measured particle number concentrations under the three flow conditions.

(ii) The normalised conditional concentration kernels are found to be largely insensitive to the flow Reynolds number that we considered, which is consistent with Ireland, Bragg & Collins (2016).

(iii) We found $\Gamma_{gh}^D \approx (1.25\text{–}1.30)\Gamma_{re}^D$ consistent with Voßkuhle, Pumir & Lévêque (2011) (i.e. ghost events overestimate the real conditional concentration rate by $\sim$30 % at small Stokes numbers).

(iv) For $r/D < 3.5$, we observe that all concentration kernels increase with r/D, which is a consequence of the inward velocity modification for $r/\eta < 1$ induced by finite-size effects, preventing particles from colliding.

4. Conclusion

Kinematic and dynamic conditional concentration kernels of solid inertialess particles in isotropic turbulence at low to intermediate Taylor Reynolds numbers with real particle diameters smaller than the Kolmogorov length scale are measured experimentally. Dynamic conditional concentration kernels are measured using 3-D PTV and fully resolved particles providing similar results with kinematic conditional concentration kernels. The high spatial resolution, large observation volume and long acquisition time allow for calculating particle relative velocity statistics over a wide range of distance r from the dissipation range to the integral scale range with 5×10^5 particle relative velocity samples in each bin. This leads to over 10^9 realisations, which allows for well-converged statistics. The particle relative velocity variance agrees well with Kolmogorov theory in the inertial subrange. For separation distances r smaller than the Kolmogorov length scale η, finite-size effects lead to a new scaling of particle relative velocity variance compared to that of fluid particles where $S_{2\parallel}^P = r\epsilon/(15\nu)$ for particle diameters $D \lesssim \eta$ provides a good approximation. We speculate that the departure from point-tracer behaviour is due to long-range interactions together with lubrication forces, whose consequences perhaps persist at those large distances.

Both kinematic and dynamic conditional concentration kernels at small separation distances are compared with Saffman & Turner (1956) theory. The deviation at small distance is attributed to finite-size effects (Ababaei *et al.* 2021), while, at larger distance, we recover the Saffman & Turner approximation. The present method allows for direct conditional concentration measurements, excluding multiple instances when the inter-particle distance falls below the distance d from the first (initial) instance for the calculation of the dynamic conditional concentration kernels. This is confirmed by $\Gamma_{gh}^D \approx (1.25\text{–}1.35)\Gamma_{re}^D$, close to the finding of Voßkuhle *et al.* (2011), which demonstrated that the 'ghost conditional concentration' approach overestimates the conditional concentration kernel by up to 30 %. Furthermore, normalised dynamic

conditional concentration kernels appear to be independent of the present Reynolds number, in agreement with Ireland *et al.* (2016). Dynamic conditional concentration kernels are based on the measurement of inter-particle distances using analogous but larger particles centred on the real particles. Further experimental work, such as the recent study by Hammond & Meng (2021), needs to focus on finite-size inertial particles, since analogous inertial particles would behave differently than real host particles near contact. Recent DNS by Ababaei *et al.* (2021) show that finite-size effects should remain an important factor when inertial particles come into contact and largely contribute to accurately estimating collision kernels.

Acknowledgements. We would like to thank A.D. Bragg, A. Liberzon, D.L. Koch and S. Xu for helpful discussions. We acknowledge Longleaf Computing Cluster at the University of North Carolina at Chapel Hill and the support provided by the ITS Research Computing and the Joint Applied Mathematics and Marine Sciences Fluids Lab of UNC-Chapel Hill. We would also like to thank the reviewers for their useful and constructive comments.

Funding. The authors acknowledge the support of the National Science Foundation Grant Numbers OCE–1335088, OCE–1155558 and OCE–1736989.

Declaration of interests. The authors report no conflict of interest.

Author ORCIDs.
Pierre-Yves Passaggia https://orcid.org/0000-0002-3607-7224;
Brian L. White https://orcid.org/0000-0002-3739-9604.

Appendix A. Estimation of the turbulent kinetic energy dissipation rate from PIV

Turbulence kinematic energy dissipation ϵ could not be directly measured from the spectra reported in figure 2(*a*) because the PIV spectra hardly resolved the Taylor microscale λ, leaving most of the turbulence kinetic energy dissipation spectrum out of reach. Instead, ϵ was estimated based on the turbulence kinetic energy budget from 2-D PIV measurements. Here, we chose a rectangular control volume, located at the position of the laser volume used for PTV and shown in figure 1. Using the divergence theorem, the quantities are projected onto the surfaces of the control volume and the turbulence kinetic energy budget simplifies to

$$\int_V \epsilon \,\mathrm{d}V = -\int_{S_x} (U\overline{k'} + \overline{u'k'})n_x \,\mathrm{d}y - \int_{S_y} (V\overline{k'} + \overline{v'k'})n_y \,\mathrm{d}x - \int_V \overline{u_i' u_j'} U_{ij} \,\mathrm{d}V, \tag{A1}$$

where ϵ is the local time-averaged turbulence kinetic energy dissipation, S_x are the faces of the control volume in the horizontal direction x while S_y is oriented in the vertical direction y. Here, the overbar denotes the temporal mean, (U, V) is the mean flow computed from all PIV snapshots and $\overline{k'}$ is the time-averaged turbulence kinetic energy. Note that the pressure–velocity diffusion term was neglected since it was not directly accessible from PIV measurements and because it plays no significant role in nearly homogeneous and isotropic turbulence (Sagaut & Cambon 2008). The spatially averaged turbulence kinetic energy dissipation rate ϵ was finally obtained by dividing the left-hand side of (A1) by the control volume V.

References

Ababaei, A., Rosa, B., Pozorski, J. & Wang, L.-P. 2021 On the effect of lubrication forces on the collision statistics of cloud droplets in homogeneous isotropic turbulence. *J. Fluid Mech.* **918**, A22.

ABRAHAMSON, J. 1975 Collision rates of small particles in a vigorously turbulent fluid. *Chem. Engng Sci.* **30** (11), 1371–1379.

AKUTINA, Y. 2016 Experimental investigation of flow structures in a shallow embayment using 3D-PTV. PhD thesis, Karlsruhe Institute of Technology.

BALACHANDAR, S. 1988 Particle coagulation in homogeneous turbulence. PhD thesis, Brown University.

BARBER, C.B., DOBKIN, D.P., DOBKIN, D.P. & HUHDANPAA, H. 1996 The quickhull algorithm for convex hulls. *ACM Trans. Math. Softw.* **22** (4), 469–483.

BEWLEY, G.P., SAW, E.-W. & BODENSCHATZ, E. 2013 Observation of the sling effect. *New J. Phys.* **15** (8), 083051.

BRAGG, A.D. & COLLINS, L.R. 2014*a* New insights from comparing statistical theories for inertial particles in turbulence: I. Spatial distribution of particles. *New J. Phys.* **16** (5), 055013.

BRAGG, A.D. & COLLINS, L.R. 2014*b* New insights from comparing statistical theories for inertial particles in turbulence: II. Relative velocities. *New J.Phys.* **16** (5), 055014.

BRENNER, H. 1961 The slow motion of a sphere through a viscous fluid towards a plane surface. *Chem. Engng Sci.* **16** (3–4), 242–251.

BRUNK, B.K., KOCH, D.L. & LION, L.W. 1998*a* Observations of coagulation in isotropic turbulence. *J. Fluid Mech.* **371**, 81–107.

BRUNK, B.K., KOCH, D.L. & LION, L.W. 1998*b* Turbulent coagulation of colloidal particles. *J. Fluid Mech.* **364**, 81–113.

CAO, L., PAN, G., DE JONG, J., WOODWARD, S. & MENG, H. 2008 Hybrid digital holographic imaging system for three-dimensional dense particle field measurement. *Appl. Opt.* **47** (25), 4501–4508.

CARNEIRO, M.V., ARAÚJO, N.A.M., PÄHTZ, T. & HERRMANN, H.J. 2013 Midair collisions enhance saltation. *Phys. Rev. Lett.* **111**, 058001.

CHEN, S. 2020 Particle collision in grid turbulence. PhD thesis, The University of North Carolina at Chapel Hill.

COX, R.G. & BRENNER, H. 1967 The slow motion of a sphere through a viscous fluid towards a plane surface—II small gap widths, including inertial effects. *Chem. Engng Sci.* **22** (12), 1753–1777.

DELICHATSIOS, M.A. & PROBSTEIN, R.F. 1975 Coagulation in turbulent flow: theory and experiment. *J. Colloid Interface Sci.* **51** (3), 394–405.

DOU, Z., BRAGG, A.D., HAMMOND, A.L., LIANG, Z., COLLINS, L.R. & MENG, H. 2018*a* Effects of Reynolds number and stokes number on particle-pair relative velocity in isotropic turbulence: a systematic experimental study. *J. Fluid Mech.* **839**, 271–292.

DOU, Z., IRELAND, P.J., BRAGG, A.D., LIANG, Z., COLLINS, L.R. & MENG, H. 2018*b* Particle-pair relative velocity measurement in high-reynolds-number homogeneous and isotropic turbulence using 4-frame particle tracking velocimetry. *Exp. Fluids* **59** (2), 30.

FLAGAN, R.C. & SEINFELD, J.H. 1988 *Fundamentals of Air Pollution Engineering*. Prentice-Hall, Inc., Dover.

GRABOWSKI, W.W. & WANG, L.-P. 2013 Growth of cloud droplets in a turbulent environment. *Annu. Rev. Fluid Mech.* **45** (1), 293–324.

GUSTAVSSON, K. & MEHLIG, B. 2011 Distribution of relative velocities in turbulent aerosols. *Phys. Rev.* E **84**, 045304.

HAMMOND, A. & MENG, H. 2021 Particle radial distribution function and relative velocity measurement in turbulence at small particle-pair separations. *J. Fluid Mech.* **921**, A16.

HILL, P.S., NOWELL, A.R.M. & JUMARS, P.A. 1992 Encounter rate by turbulent shear of particles similar in diameter to the Kolmogorov scale. *J. Mar. Res.* **50** (4), 643–668.

HOLTZER, G.L. & COLLINS, L.R. 2002 Relationship between the intrinsic radial distribution function for an isotropic field of particles and lower-dimensional measurements. *J. Fluid Mech.* **459**, 93–102.

HWANG, W. & EATON, J.K. 2004 Creating homogeneous and isotropic turbulence without a mean flow. *Exp. Fluids* **36**, 444–454.

IRELAND, P.J., BRAGG, A.D. & COLLINS, L.R. 2016 The effect of Reynolds number on inertial particle dynamics in isotropic turbulence. Part 1. Simulations without gravitational effects. *J. Fluid Mech.* **796**, 617–658.

IZARD, E., BONOMETTI, T. & LACAZE, L. 2014 Modelling the dynamics of a sphere approaching and bouncing on a wall in a viscous fluid. *J. Fluid Mech.* **747**, 422–446.

DE JONG, J., SALAZAR, J.P.L.C., WOODWARD, S.H., COLLINS, L.R. & MENG, H. 2010 Measurement of inertial particle clustering and relative velocity statistics in isotropic turbulence using holographic imaging. *Intl J. Multiphase Flow* **36** (4), 324–332.

KIM, J. & ANTONIA, R.A. 1993 Isotropy of the small scales of turbulence at low Reynolds number. *J. Fluid Mech.* **251**, 219–238.

KIØRBOE, T., ANDERSEN, K.P. & DAM, H.G. 1990 Coagulation efficiency and aggregate formation in marine phytoplankton. *Mar. Biol.* **107** (2), 235–245.
LÜTHI, B., TSINOBER, A. & KINZELBACH, W. 2005 Lagrangian measurement of vorticity dynamics in turbulent flow. *J. Fluid Mech.* **528**, 87–118.
MAAS, H.G., GRUEN, A. & PAPANTONIOU, D. 1993 Particle tracking velocimetry in three-dimensional flows. *Exp. Fluids* **15** (2), 133–146.
MARSHALL, J.S. 2011 Viscous damping force during head-on collision of two spherical particles. *Phys. Fluids* **23** (1), 013305.
MAXEY, M.R. 1987 The gravitational settling of aerosol particles in homogeneous turbulence and random flow fields. *J. Fluid Mech.* **174**, 441–465.
MCQUARRIE, D.A. 1976 *Statistical Mechanics*. Harper & Row.
MENG, H., PAN, G., PU, Y. & WOODWARD, S.H. 2004 Holographic particle image velocimetry: from film to digital recording. *Meas. Sci. Technol.* **15** (4), 673–685.
MEUNIER, P. & LEWEKE, T. 2003 Analysis and treatment of errors due to high velocity gradients in particle image velocimetry. *Exp. Fluids* **35** (5), 408–421.
MEYER, C.J. & DEGLON, D.A. 2011 Particle collision modeling – a review. *Miner. Engng* **24** (8), 719–730.
MONCHAUX, R., BOURGOIN, M. & CARTELLIER, A. 2010 Preferential concentration of heavy particles: a voronoï analysis. *Phys. Fluids* **22** (10), 103304.
MONCHAUX, R., BOURGOIN, M. & CARTELLIER, A. 2012 Analyzing preferential concentration and clustering of inertial particles in turbulence. *Intl J. Multiphase Flow* **40**, 1–18.
MONGRUEL, A., LAMRIBEN, C., YAHIAOUI, S. & FEUILLEBOIS, F. 2010 The approach of a sphere to a wall at finite Reynolds number. *J. Fluid Mech.* **661**, 229–238.
PAN, L. & PADOAN, P. 2010 Relative velocity of inertial particles in turbulent flows. *J. Fluid Mech.* **661**, 73–107.
PAN, L. & PADOAN, P. 2014 Turbulence-induced relative velocity of dust particles. IV. The collision kernel. *Astrophys. J.* **797** (2), 101.
PASSAGGIA, P.-Y., CHALAMALLA, V.K., HURLEY, M.W., SCOTTI, A. & SANTILLI, E. 2020 Estimating pressure and internal-wave flux from laboratory experiments in focusing internal waves. *Exp. Fluids* **61** (11), 238.
PASSAGGIA, P.-Y., LEWEKE, T. & EHRENSTEIN, U. 2012 Transverse instability and low-frequency flapping in incompressible separated boundary-layer flows: an experimental study. *J. Fluid Mech.* **703**, 363–373.
PETERSON, A.J., BAKER, L. & COLETTI, F. 2019 Experimental study of inertial particles clustering and settling in homogeneous turbulence. *J. Fluid Mech.* **864**, 925–970.
ROSA, B., PARISHANI, H., AYALA, O., GRABOWSKI, W.W. & WANG, L.-P. 2013 Kinematic and dynamic collision statistics of cloud droplets from high-resolution simulations. *New J. Phys.* **15** (4), 045032.
SAFFMAN, P.G. & TURNER, J.S. 1956 On the collision of drops in turbulent clouds. *J. Fluid Mech.* **1** (1), 16–30.
SAGAUT, P. & CAMBON, C. 2008 *Homogeneous Turbulence Dynamics*, vol. 10. Springer.
SAW, E.-W., BEWLEY, G.P., BODENSCHATZ, E., RAY, S.S. & BEC, J. 2014 Extreme fluctuations of the relative velocities between droplets in turbulent airflow. *Phys. Fluids* **26** (11), 111702.
SQUIRES, K.D. & EATON, J.K. 1991 Preferential concentration of particles by turbulence. *Phys. Fluids* **3** (5), 1169–1178.
SUNDARAM, S. & COLLINS, L.R. 1996 Numerical considerations in simulating a turbulent suspension of finite-volume particles. *J. Comput. Phys.* **124** (2), 337–350.
SUNDARAM, S. & COLLINS, L.R. 1997 Collision statistics in an isotropic particle-laden turbulent suspension. Part 1. Direct numerical simulations. *J. Fluid Mech.* **335**, 75–109.
TAVOULARIS, S., BENNETT, J.C. & CORRSIN, S. 1978 Velocity-derivative skewness in small Reynolds number, nearly isotropic turbulence. *J. Fluid Mech.* **88** (1), 63–69.
TEN CATE, A., DERKSEN, J.J., PORTELA, L.M. & VAN DEN AKKER, H.E.A. 2004 Fully resolved simulations of colliding monodisperse spheres in forced isotropic turbulence. *J. Fluid Mech.* **519**, 233–271.
VASSILICOS, J.C. 2015 Dissipation in turbulent flows. *Annu. Rev. Fluid Mech.* **47**, 95–114.
VOSSKUHLE, M., PUMIR, A. & LÉVÊQUE, E. 2011 Estimating the collision rate of inertial particles in a turbulent flow: limitations of the 'ghost collision' approximation. *J. Phys.: Conf. Ser.* **318** (5), 052024.
WANG, L.-P., FRANKLIN, C.N., AYALA, O. & GRABOWSKI, W.W. 2006 Probability distributions of angle of approach and relative velocity for colliding droplets in a turbulent flow. *J. Atmos. Sci.* **63** (3), 881–900.
WANG, L.-P., WEXLER, A.S. & ZHOU, Y. 1998 On the collision rate of small particles in isotropic turbulence. I. Zero-inertia case. *Phys. Fluids* **10** (1), 266–276.
WANG, L.-P., WEXLER, A.S. & ZHOU, Y. 2000 Statistical mechanical description and modelling of turbulent collision of inertial particles. *J. Fluid Mech.* **415**, 117–153.

WILLNEFF, J. 2003 A spatio-temporal matching algorithm for 3D particle tracking velocimetry. PhD thesis, ETH Zurich.

XIONG, Y. & PRATSINIS, S.E. 1991 Gas phase production of particles in reactive turbulent flows. *J. Aerosp. Sci.* **22** (5), 637–655.

YANG, F.-L. & HUNT, M.L. 2006 Dynamics of particle–particle collisions in a viscous liquid. *Phys. Fluids* **18** (12), 121506.

ZAICHIK, L.I. & ALIPCHENKOV, V.M. 2009 Statistical models for predicting pair dispersion and particle clustering in isotropic turbulence and their applications. *New J. Phys.* **11** (10), 103018.